

Article

Structural, Optical, Electrical and Antibacterial Properties of Fe-Doped CeO₂ Nanoparticles

Shalendra Kumar^{1,2,*}, Suliman Yousef AlOmar^{3,*}, Kavita Kumari⁴, Fadwa Albalawi³, Rajesh Kumar^{5,*}, Faheem Ahmed¹, Naushad Ahmad⁶, Sourabh Dwivedi⁷ and Parvez Ahmad Alvi⁸

¹ Department of Physics, College of Science, King Faisal University, P.O. Box 400, Hofuf 31982, Saudi Arabia; fahmed@kfu.edu.sa

² Department of Physics, University of Petroleum & Energy Studies, Dehradun 248007, India

³ Department of Zoology, King Saud University, Riyadh 11451, Saudi Arabia; Fadwa_saad@hotmail.com

⁴ School of Materials Science and Engineering, Changwon National University, Changwon 51140, Korea; kkmalhan@gmail.com

⁵ University School of Basic and Applied Sciences, Guru Gobind Singh Indraprastha University, New Delhi 110078, India

⁶ Chemistry Department, College of Science, King Saud University, Riyadh 11451, Saudi Arabia; anaushad@ksu.edu.sa

⁷ Department of Applied Physics, Aligarh Muslim University, Aligarh 202001, India; sourabh25june@gmail.com

⁸ Department of Physics, Banasthali Vidyapith, Banasthali 304022, India; parveznihal@gmail.com

* Correspondence: sjagdish@kfu.edu.sa (S.K.); syalomar@ksu.edu.sa (S.Y.A.); rajeshpositron@gmail.com (R.K.)



Citation: Kumar, S.; AlOmar, S.Y.; Kumari, K.; Albalawi, F.; Kumar, R.; Ahmed, F.; Ahmad, N.; Dwivedi, S.; Ahmad Alvi, P. Structural, Optical, Electrical and Antibacterial Properties of Fe-Doped CeO₂ Nanoparticles. *Crystals* **2021**, *11*, 1594. <https://doi.org/10.3390/cryst11121594>

Academic Editor: Marilena Carbone

Received: 31 October 2021

Accepted: 13 December 2021

Published: 20 December 2021

Publisher's Note: MDPI stays neutral with regard to jurisdictional claims in published maps and institutional affiliations.



Copyright: © 2021 by the authors. Licensee MDPI, Basel, Switzerland. This article is an open access article distributed under the terms and conditions of the Creative Commons Attribution (CC BY) license (<https://creativecommons.org/licenses/by/4.0/>).

Abstract: This paper reports the structural, optical and antimicrobial study of Ce_{1-x}Fe_xO_{2-δ} (0 ≤ x ≤ 20) nanoparticles (NPs) synthesized using a microwave-assisted hydrothermal method. The XRD pattern analysed using Rietveld refinement method clearly infers that all the samples exhibit single phase nature and exclude the possibility of an impurity phase. The lattice parameters and unit cell volume were found to decrease with an increase in Fe-doping content in CeO₂ nanoparticles. The crystalline size determined using XRD pattern and TEM micrographs was found to decrease with Fe doping in CeO₂. Selective area electron diffraction (SAED) pattern also demonstrated the crystalline nature of the Fe-CeO₂ nanoparticles. Optical properties studied using UV-vis spectroscopy indicated that band gap decreased with an increase in Fe doping. The electrical properties have been investigated via dielectric constant, dielectric loss and AC conductivity. The dielectric constant was found to increase in the Fe-doped CeO₂ nanoparticles, while AC conductivity was found to be reduced, which shows good dielectric behaviour of the Fe-doped CeO₂ nanoparticles. The antibacterial activity of the synthesized NPs was achieved under ambient conditions with different bacteria, and the results showed that the properties were different for both bacteria. The antimicrobial activity reflects the possibility to develop Fe-doped CeO₂ NPs as antibacterial agents against extensive microorganisms to control and prevent the spread and persistence of bacterial infections.

Keywords: CeO₂; XRD; UV-vis; antibacterial

1. Introduction

Cerium is a rare earth element of the lanthanide series which is found in abundant amounts in the Earth's crust. It exists in dual oxidation states—Ce⁺³ and Ce⁺⁴ [1–3]. Cerium dioxide (CeO₂) has attracted significant attention due to diverse structural, optical, magnetic, and antimicrobial properties in a wide range of applications in different fields [4–8]. The swapping of the oxidation state from +3 to +4 state and vice versa is due to quick gain or release of oxygen through oxidation and reduction reactions due to which it can store and transport oxygen [9,10]. These distinctive properties of CeO₂ make it a prominent material for various magnetic, catalytic, and industrial applications. CeO₂ becomes a reactive element because of its interchangeable states, which makes it relevant for catalytic

purposes [11]. CeO₂ is also well acknowledged for its other applications in spintronic devices, optoelectronics, gas sensors, cosmetic products, water splitting, solar cell devices, solid oxide fuel cells, and many more. Due to a wide bandgap, CeO₂ has been considered as a prominent candidate, among which defects, disorders, and nonstoichiometry are recognized as the key features for its magnetism. The involvement of transition metals (TM) and rare earth (RE) elements in host material has increased professionals' interest in it. The addition of TM/RE elements, such as Fe, Cu, Ni, Cr, Mn, Co, Gd, Sm, Eu, Nd and Pr as a dopant, has been reported as a significant change in the structural parameters, increasing the creation of Ce⁺³ states and oxygen vacancies in CeO₂ [7]. In recent years, it has been found that the nano-sized materials are making remarkable contributions to the medical industry in the form of imaging, combating bacterial pathogens, drug delivery, etc. [12–14]. In addition, the nanoscale antimicrobial agents have a long-lasting effect on the living systems as compared to conventional molecular antimicrobial agents [12,15]. It is remarkable that, as the size of the material is reduced to nanoscale, their surface to volume ratio increases. This high surface-to-volume ratio increases the chemical reactivity of the particles and enables them to perform as efficient catalysts and antibacterial agents. This attribute of nanoparticles has been utilized in the treatment of various infectious microorganisms such as *Escherichia coli*, *Candida albicans*, etc., which form biofilms on the affected surfaces. These bacterial biofilms are developed when the bacteria inhabit the biomedical surfaces, resulting in microbial infections. The cure for such infections can be found in the nanoparticles of metal oxides such as TiO₂, ZnO, MgO, CeO₂, etc., exhibiting antibacterial properties [15,16]. Since the last few decades, researchers have been working on developing biocompatible and non-toxic nanomaterials which can be seen as a possible cure for various bacterial infections [17,18]. From the above-mentioned metal oxides, CeO₂ is one such material that has proven its effectiveness in various processes such as photocatalytic activity, water treatment and as an antibacterial material [15,19]. The dual oxidation states of CeO₂ (Ce³⁺/Ce⁴⁺) associates with excellent redox properties. The interchangeable oxidation states change the valence of Ce at the surface of the particle and expedite the chemical reaction with the surrounding environment such as the membrane of the bacterial cell. Thereby, the biologically active CeO₂ nanoparticles can be developed to treat bacterial infections. The nanoparticles utilize various effective mechanisms to degrade bacteria as compared to conventional antibiotics [13]. The treatment followed by CeO₂ nanoparticles-based antibiotics is a mechanism involving the development of the oxidative stress as addressed by Isabela, et. al [15]. The pH value of the nanoparticles is kept low in order to preserve their acidic nature because the acidic nature of CeO₂ favours the adsorption of the nanoparticles on the cell membrane of the bacteria. During adhesion, the valence state of Ce changes and develops oxidative stress on the cell membrane. This mechanism works well in Gram-negative bacteria such as *E. coli* [15,20]. However, Alpaslan et al. have shown that CeO₂ nanoparticles are more effective at higher pH values to kill bacteria [13].

The antibacterial activity of CeO₂ nanoparticles has been reported by various groups of researchers against many bacterial pathogens such as *Pseudomonas aeruginosa* (Gram-negative), *Staphylococcus epidermidis* (Gram-positive), *Staphylococcus aureus* (Gram-positive) etc. [13,21]. The nanoparticles have been found to effectively reduce the growth of *P. aeruginosa* and *S. epidermidis*. The free radicals formed at the surface of the nanoparticles interacted with the bacteria cell causing degradation. However, the nanoparticles were not detected to affect *S. aureus* [21]. Furthermore, there are various ways to enhance the antibacterial activity of CeO₂ nanoparticles such as use of surfactants or doping with transition metal ions, etc. Cuahtecontzi-Delint et al. have shown the effects of various surfactants on the antibacterial activity of CeO₂ and reported an enhancement of this property against *E. Coli* bacteria. However, sometimes the interaction of nanoparticles with the surfactants can also produce a toxic response [22]. Further, Pelletier et al. have also reported the interaction of CeO₂ nanoparticles with the *E. coli* (Gram-negative), *Shewanella oneidensis* (Gram-negative) and *Bacillus subtilis* (Gram-positive) microorganisms. The

nanoparticles were found to inhibit the growth of *E. coli* and *S. oneidensis*, although the effect is size dependent. However, *B. subtilis* remained unaffected [12]. From the above literature review, it is evident that CeO₂ nanoparticles can effectively interact with some bacterial pathogens such as *E. Coli*, *S. epidermidis*, while leaving other bacteria completely unaffected, such as *B. subtilis*, irrespective of whether the bacteria is Gram-positive or Gram-negative. However, the interaction has certainly been found to be dependent on other factors such as size of the nanoparticles, pH value or the time of treatment, etc. It has been observed through various studies that doping of CeO₂ with various transition metal ions increases their physical, optical, and photocatalytic properties [23]. For instance, Co-, Ag-, and Au-doped CeO₂ has been previously investigated for anti-bacterial and anti-cancer cells [24,25]. This leads to the expectation that its antibacterial properties can also be enhanced through doping CeO₂ with Fe, because iron oxide is known to efficiently inhibit the bacteria [13]. Therefore, in this research work, Fe-doped CeO₂ nanoparticles have been synthesized via a chemical root method in an Ar-annealed environment. The metal nitrates were used as precursors to optimize the antibacterial properties of the Fe-doped CeO₂ nanoparticles. The nitrates of the salts were used deliberately, owing to their greater solubility to make a homogeneous solution. The prepared nanoparticles were characterized for structural and antibacterial properties.

2. Experimental

Ce_{1-x}Fe_xO_{2-δ}, (0 ≤ x ≤ 20) NPs were prepared using a co-precipitation technique. This method requires a chemical reaction between the precursors, followed by stirring. The iron nitrate nonahydrate and cerium nitrate hexahydrate were taken as precursors. The stoichiometric amount of the salts was mixed in 50 mL de-ionized water to attain a solution of 0.04 M. The thus-obtained solution was kept stirring at room temperature. After half an hour of stirring, the ammonia solution was decanted dropwise whilst stirring the solution, until the pH level became 9. The colour of the solution changed with dopant concentration. The stirring continued for 3 h at room temperature at 5000 rpm. The stirring provided homogeneous mixing to the solution. Then, the mixture was centrifuged at 5000 × g rpm to collect the precipitates. Finally, the precipitates were washed three times with de-ionized water and two times with ethanol and then dried at 80 °C for 12 h. The dried precipitates were collected in a pastel mortar and ground to make fine powder, which was kept in the furnace for annealing at 500 °C for 5 h.

2.1. Samples Characterizations

The effect of Fe doping in host CeO₂ was studied using various characterization techniques, the XRD patterns were scanned using Philips X-pert X-ray diffractometer with radiation of wavelength ~1.5418 Å (Cu Kα). The particle size was calculated using Scherrer's equation. Morphological measurements were performed using FETEM (JEM 2100F) transmission electron microscope. To record the UV-visible optical spectra, S-4100 (SINCO Instrument Co., Seoul, Korea) photo spectrometer was used in the wavelength range of 200–800 nm at room temperature. The dielectric properties have conveyed out using Alpha-A High-Performance Frequency Analyser at room temperature in the frequency range from 1.0 Hz to 10 MHz.

2.2. Growth Kinetic Analysis and Biofilm Formation in A 96-Well Microplate

Initially, effects of interaction pattern at NPs-bacteria interface were studied by following growth kinetics of *S. aureus* in absence and presence NPs concentrations in the range between 20–50 µg/mL. Test organisms were prepared in LB broth, taking loop full of bacteria from the specified slant culture and were cultured overnight at 37 °C and 180 rpm agitation. The stock solutions were prepared by dispersing NPs in sterilized LB and were sonicated for 10 min followed by UV radiation sterilization before use. The reaction mixtures without NPs were taken as controls. Briefly, 20 µL of bacterial cultures were added to the different reaction mixtures prepared in a 96-well plate, and the reaction volumes

were adjusted by LB broth with NPs. Upon addition of the NP, data collection for growth kinetic studies were immediately performed by measuring optical density (O.D.) at 620 nm using a plate reader (Thermo scientific Multiskan EX, REF 51118170, China) at regular time intervals. The biofilm inhibition assay was performed according to Dwivedi et al., 2014. The microtiter plates were incubated under stationary conditions at 37 °C for 3 days. At an interval of every 28 h for 3 days, the medium was discarded from each well. The wells were then treated with a 0.1% aqueous solution of crystal violet (1 mL). The solution was washed with water, and the remaining stain was solubilized with 2 mL of 95% ethanol. Biofilm inhibition was quantified by measuring the OD570 into quartz cuvette for analysis. The assays were performed in triplicate manner.

3. Results and Discussion

The XRD patterns of $\text{Ce}_{1-x}\text{Fe}_x\text{O}_{2-\delta}$, ($0 \leq x \leq 20$) NPs, synthesized using the co-precipitation method, are highlighted in Figure 1a. The XRD pattern of Fe-doped CeO_2 nanoparticles was analysed by means of a Rietveld refinement process via FullProf open-access program [2]. The pattern with solid black spheres highlights the experimentally observed curve, and the red line superimposed onto the experimental curve shows the calculated spectra. The blue line spectra represent the difference between experimental and theoretical spectra. The Bragg's positions are shown by the pink-coloured vertical line. All the peaks in the XRD pattern were observed at the Bragg's position. Therefore, results of the Rietveld refinement clearly infer that Fe-doped CeO_2 nanoparticles exhibit the single-phase nature that rule out the any possibility of a secondary phase. The various structural parameters, such as lattice parameter (a) and lattice volume (V), and the reliability parameters, for example the Bragg R factor (R_{wp}), profile factor (R_p), expected weighted profile factor (R_{exp}) and weighted profile factor (R_{wp}), are represented in Table 1. The goodness factors of the fitting (χ^2) $\text{Ce}_{1-x}\text{Fe}_x\text{O}_{2-\delta}$, ($0 \leq x \leq 20$) NPs were found in the 0.28–1.15 range, which clearly validates the merit of the refinement. Additionally, all the peaks were observed at Bragg reflections, which are consistent with the standard peaks of CeO_2 fluorite-type structure with $Fm\bar{3}m$ (O_{5h}) space group, and in accordance with JCPDS card no. 34-039. Figure 1b demonstrates the cubic fluorite unit cell structure which is plotted from the crystallographic information file (CIF). The CIF file was obtained from the Rietveld refinement process of the XRD pattern. The various structural parameters determined using the Rietveld refinement process are listed in Table 1. It was observed that lattice parameters and unit cell volume were found to decrease from 5.417 to 5.392 Å, and from 158.99 to 156.80 Å³, respectively. The decrease in lattice parameter was due to the difference in the ionic radii of Fe^{2+} ions (ionic radii ~0.74 Å) and Ce^{4+} ions (ionic radii ~0.97 Å) [26]. Furthermore, the broadening of XRD peaks clearly indicates the nanocrystalline behaviour of $\text{Ce}_{1-x}\text{Fe}_x\text{O}_{2-\delta}$, ($0 \leq x \leq 20$) NPs. The average crystallite size was measured using the Scherrer's equation; $D = \frac{k\lambda}{\beta \cos\theta}$, where k is the shape factor with a constant value ≈ 0.9 , D is the crystallite size, λ is the wavelength used for measuring the XRD pattern, β is full width at half maxima (FWHM) of the spectral peaks, and θ is the Bragg's angle [27]. The average crystallite size ranges from 6.33 to 5.50 nm, which is consistent with previously reported results by other groups [23,28]. The variation of the lattice parameter, volume and particle size with the doping concentration of $\text{Ce}_{1-x}\text{Fe}_x\text{O}_{2-\delta}$, ($0 \leq x \leq 20$) NPs is displayed in Figure 2. The decrease in the lattice parameters and particles may also cause strain; therefore, strain in $\text{Ce}_{1-x}\text{Fe}_x\text{O}_{2-\delta}$, ($0 \leq x \leq 20$) NPs have been evaluated using Williamson–Hall's equation ($\beta = 4\epsilon \tan\theta$). It was observed that the strain was found to increase with Fe from 1.33×10^{-3} to 1.55×10^{-3} . Similar results were also reported by Dave et al. [27], where they were found to increase in strain with an increase in Nd doping in CeO_2 nanoparticles.

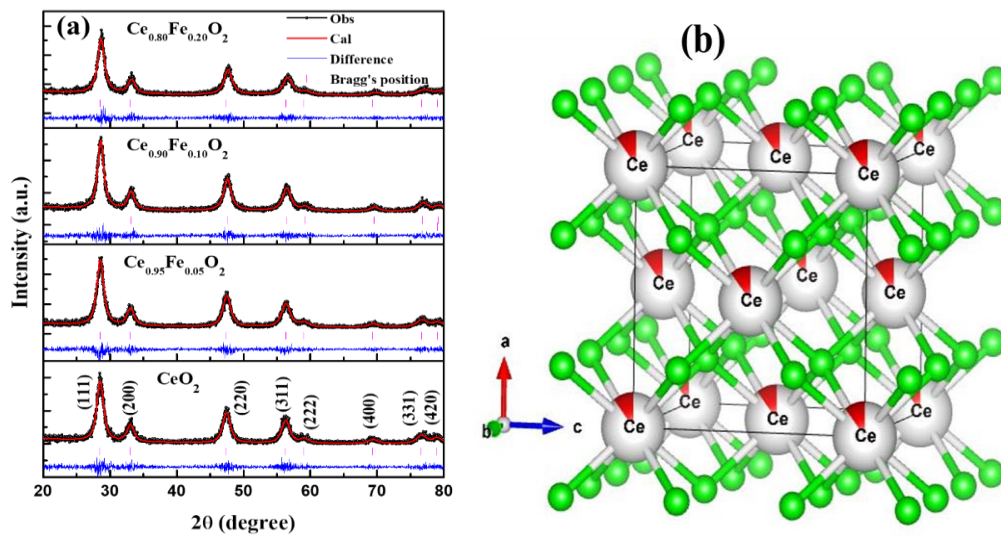


Figure 1. (a) Rietveld refinement of the XRD patterns of $\text{Ce}_{1-x}\text{Fe}_x\text{O}_{2-\delta}$, ($0 \leq x \leq 20$) NPs, (b) Representation of unit cell structure of $\text{Ce}_{0.80}\text{Fe}_{0.20}\text{O}_{2-\delta}$ nanoparticles.

Table 1. The structural parameters obtained from Rietveld refinement of the XRD patterns.

	CeO_2	$\text{Ce}_{0.95}\text{Fe}_{0.05}\text{O}_2$	$\text{Ce}_{0.90}\text{Fe}_{0.10}\text{O}_2$	$\text{Ce}_{0.80}\text{Fe}_{0.20}\text{O}_2$
Strain (10^{-3})	1.30	1.40	1.45	1.50
Density (ρ_{th})	7.396 g/cm ³	7.390 g/cm ³	7.392 g/cm ³	7.793 g/cm ³
Specific surface area (S_a) $\times 10^5$	13.0	14.0	12.0	14.0
R-Factors	5.20	1.38	1.33	0.647
Bragg R-factor	7.51	3.19	1.89	1.30
χ^2	1.15	0.446	0.278	0.2150
R_p	21.5	20.5	21.0	21.8
R_{wp}	29.7	21.1	19.3	19.4
R_{exp}	27.65	31.6	36.6	41.8

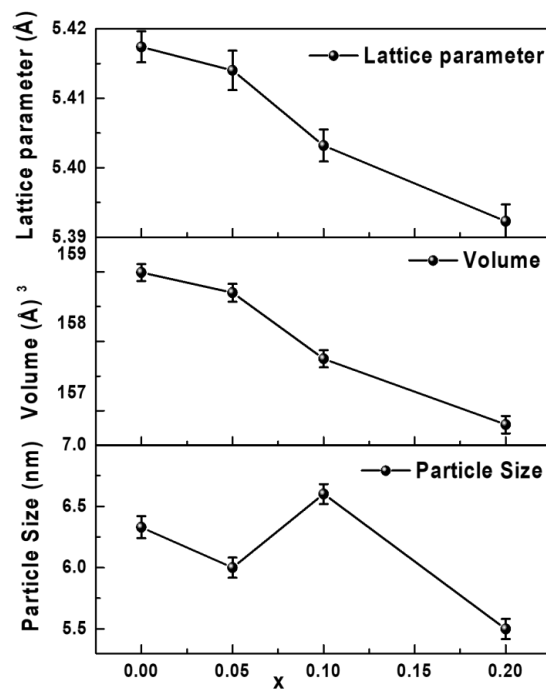


Figure 2. Variation of lattice parameter, volume and particle size with the doping concentration of $\text{Ce}_{1-x}\text{Fe}_x\text{O}_{2-\delta}$, ($0 \leq x \leq 20$) NPs.

Surface morphology and particle size of $\text{Ce}_{1-x}\text{Fe}_x\text{O}_{2-\delta}$, ($0 \leq x \leq 10$) NPs were further investigated by means of field emission transmission electron microscopy. Figure 3a–f elucidates the uniform morphological characterization of $\text{Ce}_{1-x}\text{Fe}_x\text{O}_{2-\delta}$, ($0 \leq x \leq 10$) NPs. The transmission electron micrographs show a broad distribution of particles. TEM micrograph shows that $\text{Ce}_{1-x}\text{Fe}_x\text{O}_{2-\delta}$, ($0 \leq x \leq 10$) NPs have moderate agglomeration with quasi-spherical shapes. The particle size observed for undoped CeO_2 was 6.33 nm and decreased to 5.5 nm with Fe doping. The decrease in particle size may also increase the surface-to-volume ration. The specific surface area (S_a) was calculated using the relation $S_a = \frac{6}{D \times \rho} \frac{\text{cm}^2}{\text{gm}}$, which was found to increase with an increase in Fe doping in CeO_2 nanoparticles. The particle size also affected the crystal quality, and it was reported by some groups that a decrease in particles may enhance the oxygen vacancies-related defect as well as the deformation of surface texture [26]. Furthermore, the crystal structure of the Fe-doped CeO_2 nanoparticles was studied using the selective area electron diffraction method (SAED). The SAED pattern was captured by focusing the electron onto nanoparticles. It can be clearly seen from the SAED pattern, as shown in Figure 3e–g, that prepared nanoparticles demonstrate single-phase nature and that results are in good agreement with XRD.

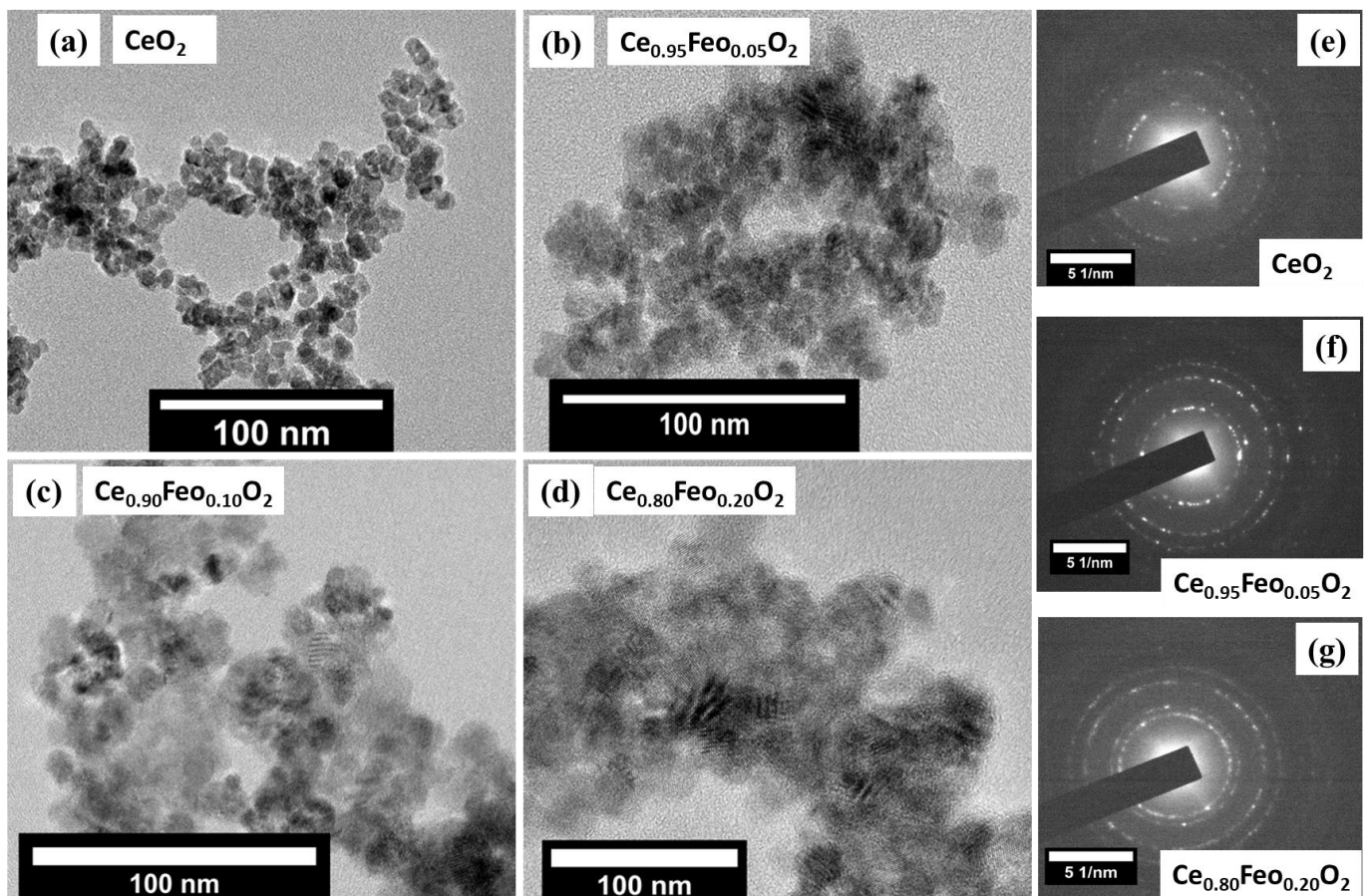


Figure 3. TEM micrographs of (a) CeO_2 , (b) $\text{Ce}_{0.95}\text{Fe}_{0.05}\text{O}_2$, (c) $\text{Ce}_{0.90}\text{Fe}_{0.10}\text{O}_2$, (d) $\text{Ce}_{0.80}\text{Fe}_{0.20}\text{O}_2$ NPs. SAED patterns of (e) CeO_2 , (f) $\text{Ce}_{0.95}\text{Fe}_{0.05}\text{O}_2$, (g) $\text{Ce}_{0.80}\text{Fe}_{0.20}\text{O}_2$ NPs.

UV–vis absorption spectroscopy has been employed to investigate the optical properties of $\text{Ce}_{1-x}\text{Fe}_x\text{O}_{2-\delta}$, ($0 \leq x \leq 20$) NPs. Figure 4a demonstrates the optical responses of $\text{Ce}_{1-x}\text{Fe}_x\text{O}_{2-\delta}$, ($0 \leq x \leq 20$) NPs. The absorption bands have shifted towards higher wavelengths as the Fe concentration increases, indicating a decrease in the band gap energy. The direct band gap energy was extracted by using the following equation: $(\alpha h\nu)^2 = B(h\nu - E_g)$,

where $h\nu$ is the absorbed photon energy; $h\nu = \frac{1241}{\lambda(\text{nm})}$ (eV), α is the absorption coefficient, B is a constant [29]. The slope of the $(\alpha h\nu)^2$ Vs $h\nu$ curve gives the band gap energy for the particular sample, as shown in Figure 4b, where the straight line intercepts on the x-axis. The band gap energy for undoped CeO_2 is found to be 2.6 eV, which surprisingly increases for 1% Fe doping (5.3 eV) but then decreases for higher concentrations of Fe in CeO_2 (3.7 eV for 20% doped CeO_2), as shown in Figure 4b. This decreasing band gap with increasing Fe-concentration points towards the role of 3d transition metal orbitals as well as V_o that might be induced by Fe doping. H. Shi et al. have shown in their ab initio calculations for density of states (DOS) that doping of non-TM atoms such as C, N, P and S, including rare earth elements such as La and Pr also reduced the band gap, although they do not have any 3d orbitals [10]. It is argued that the dopant increases the density of electrons in the valence band in association with V_o induced by Fe ions, which causes a release of more electrons. Therefore, we can say that the V_o plays an important role in lowering the energy and bridging the gap between the valence band and conduction band.

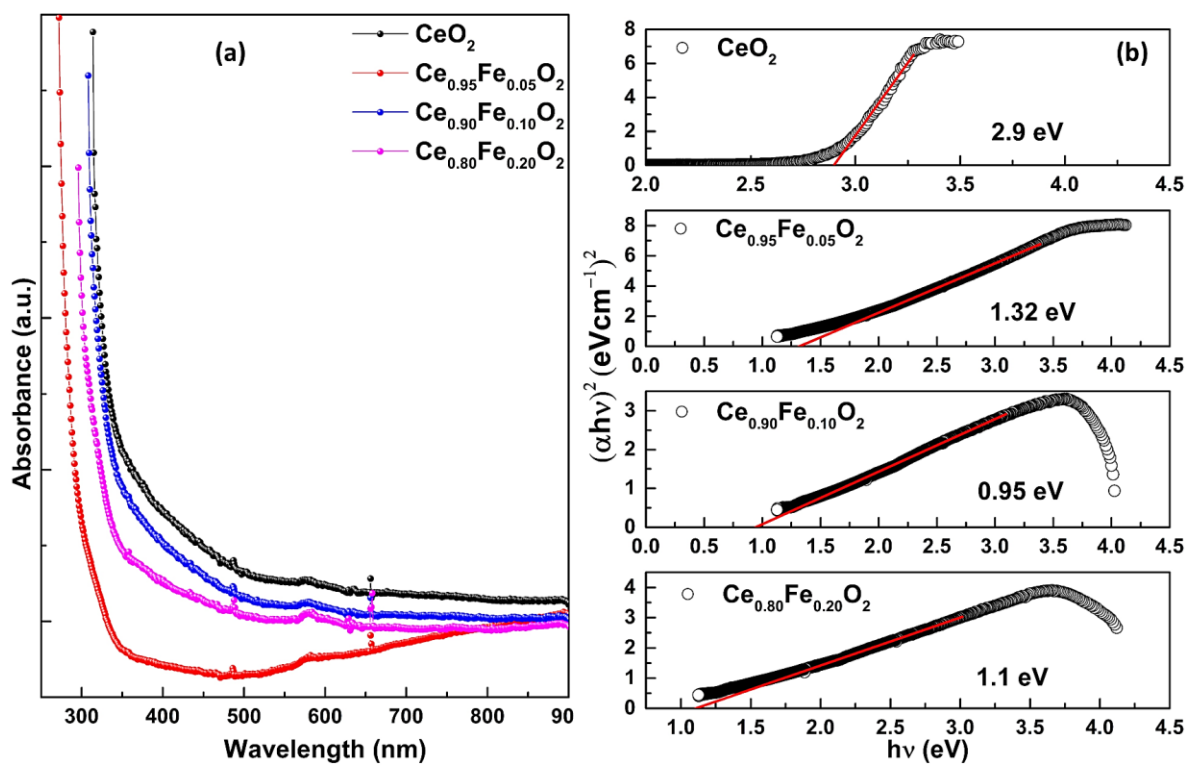


Figure 4. (a) Absorption curves and (b) $(\alpha h\nu)^2$ vs $(h\nu)$ plots of $\text{Ce}_{1-x}\text{Fe}_x\text{O}_{2-\delta}$, ($0 \leq x \leq 20$) NPs.

The influence of Fe dopant on the dielectric properties, such as real part of dielectric constant (ϵ'), loss tangent ($\tan\delta$), and ac conductivity (σ_{ac}) of CeO_2 NPs, has been studied at room temperature in the 1.0 Hz to 10 MHz frequency range. Figure 5 demonstrates the variation of the dielectric constant (ϵ') with frequency for Fe-doped CeO_2 nanoparticles at room temperature. The value of the dielectric constant (ϵ') was calculated using the relation: $\epsilon' = \frac{Cd}{\epsilon_0 A}$, where C , A and d are the capacitance, area and thickness of the pallet, respectively, and ϵ_0 is the permittivity of free space. The dielectric constant gives information about the energy stored in the material [30–33]. It can be observed that the dielectric constant decreases with increasing frequency and becomes almost constant above ~ 1000 Hz. At a lower frequency region, the value of the dielectric constant is attributed to molecular polarization, which can oscillate and align in the presence of an externally applied field. When the frequency is low, the dipoles can oscillate in accordance with this frequency; however, when the frequency is increased beyond a certain value (~ 1000 Hz in the present case), the dipoles fail to align along the frequency of the applied field. Owing to this, the

dielectric constant exhibits almost constant behaviour at higher frequencies, indicating an increase in the relaxation time of the polarization. Therefore, the constant behaviour of the dielectric constant at higher frequencies indicates that the dielectric constant becomes almost independent of frequency. Further, it has been observed that the value of the dielectric constant at 1 Hz is maximum for pure CeO_2 and reduces as the Fe concentration increases to 5% and 10%. However, at 20% Fe concentration, the initial value of the dielectric constant at 1 Hz increases and becomes comparable to that of the pure CeO_2 . This is because as the concentration of Fe^{2+} ions increases, the charge compensation increases due to substitution of Fe^{2+} in place of Ce^{4+} ions. The enhanced charge compensation increases availability of the free charge carriers, which further enhances the space charge polarization. Due to an increase in the space charge polarization, the value of the dielectric constant increases [34]. The values of the dielectric constant obtained in the present case are significantly higher than the earlier reported values. For instance, Bandyopadhyaya et al. have reported the values of the dielectric constant for $\text{Ce}_{0.90}\text{Gd}_{0.10}\text{O}_{2-\delta}$ to be ~ 150 and below at different temperatures [35]. However, in our case, the values of the dielectric constant for all the samples are above 1000 and extend to 6000. Additionally, this reveals that Fe is more favourable than Gd for the enhancement of dielectric properties of the material.

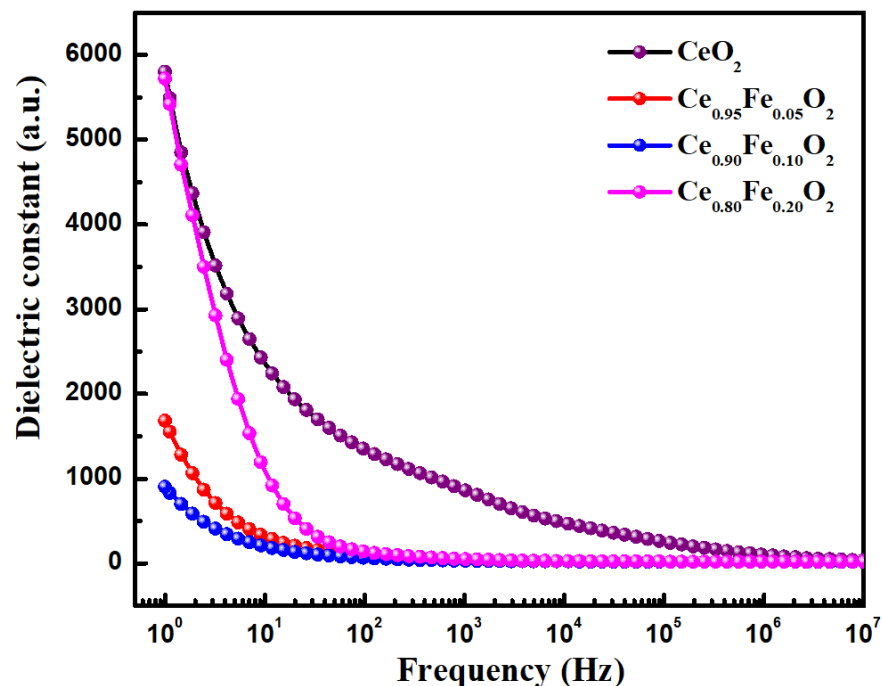


Figure 5. Dielectric constant vs. frequency of $\text{Ce}_{1-x}\text{Fe}_x\text{O}_{2-\delta}$, ($0 \leq x \leq 20$) NPs at room temperature.

The variation of dielectric loss with frequency is demonstrated by the loss tangent $\tan \delta$ vs frequency curve, as shown in Figure 6. The dielectric loss gives information about the energy lost in the form of heat and has been measured as: $\tan \delta = \epsilon'' / \epsilon'$ [36,37]. It was observed that the dielectric losses are higher at lower frequencies, which decreases with increasing frequency. The higher dielectric losses at lower frequencies can be identified as a well-defined peak which is governed by the equation: $\omega_{\max} \cdot \tau = 1$, with τ as the Debye relaxation [38]. As the frequency increases, the dielectric loss reduces; however, the reducing behaviour of Fe-doped CeO_2 is different than the undoped CeO_2 . This indicates that dielectric relaxation phenomena are modified as a consequence of Fe doping in the samples, decreasing linearly at higher frequencies as compared to the undoped CeO_2 . However, the curves exhibit a non-monotonic behaviour at lower frequencies, which may be due to the increasing concentration of Fe ions in the host matrix. The authors have previously investigated the Fe-doped CeO_2 system with various conditions and found

that the Fe dissolved in the CeO_2 matrix in mixed valence states ($\text{Fe}^{2+}/\text{Fe}^{3+}$) [39,40]. The increase in $\text{Fe}^{2+}/\text{Fe}^{3+}$ ions with increasing doping concentration may be associated with the observed non-monotonic behaviour at lower frequencies. All the samples exhibited Debye-type relaxation.

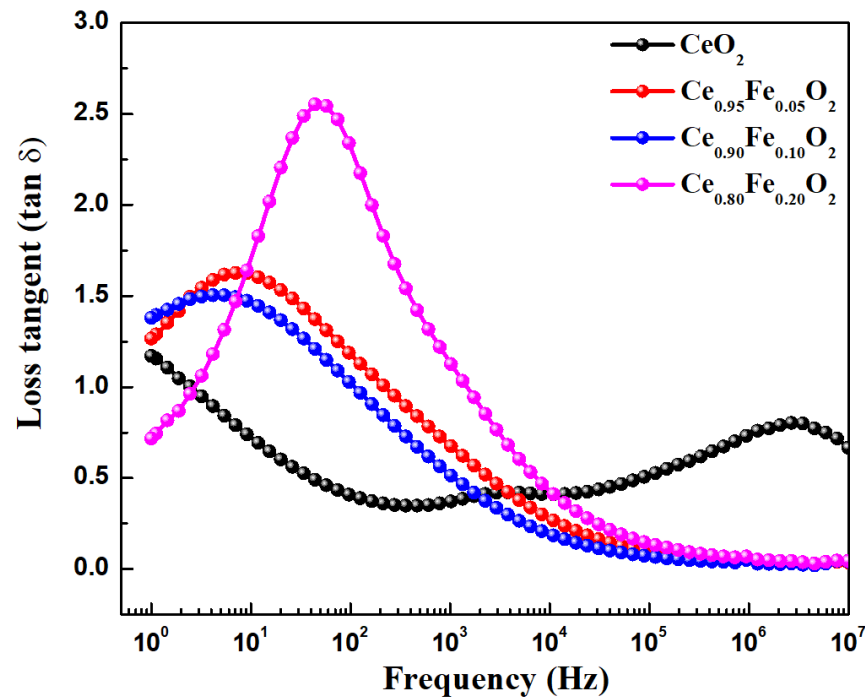


Figure 6. Loss tangent ($\tan \delta$) vs. frequency of $\text{Ce}_{1-x}\text{Fe}_x\text{O}_{2-\delta}$, ($0 \leq x \leq 20$) NPs at room temperature.

The determination of AC conductivity (σ_{AC}) as a function of frequency was investigated using the formula: $\sigma_{AC} = \epsilon' \epsilon_0 \omega \tan \delta$, the meaning of symbols has already been described above in the section [41]. The AC conductivity Vs frequency curves are displayed in Figure 7a, demonstrating that AC conductivity increases almost linearly with the frequency for undoped CeO_2 . However, it has been observed that for Fe-doped CeO_2 , AC conductivity varies linearly with frequency at lower frequencies (<100 Hz), but it deviates from linearity at higher frequencies and shows slow variation. In addition, the difference of AC conductivity between the undoped and doped samples is negligible at lower frequencies and increases with the increase of frequencies. At higher frequencies, it becomes quite significant. To further understand the relationship between AC conductivity and frequency, the curves have been fitted using the equation: $\sigma_{AC} = A\omega^s$, where A is the constant, while s is the frequency exponent [41]. The frequency exponent “s” is an important factor that describes the degree of correlation of AC conductivity with the frequency. The linearly fitted curves between $\ln(\sigma_{AC})$ and $\ln(\omega^s)$ are displayed in Figure 7b. The values of the exponent ‘s’ are displayed in the figure along with the respective curve. It can be observed that the value of ‘s’ decreases as the Fe concentration in the sample increases. The decrease in the value of s indicates towards the decrease in the directly proportional relationship of AC conductivity with the frequency. The reduction of conductivity in the doped samples is in accordance with the enhanced dielectric constant. The increase in the dielectric constant increases the polarization, which reduces the conductivity of the material.

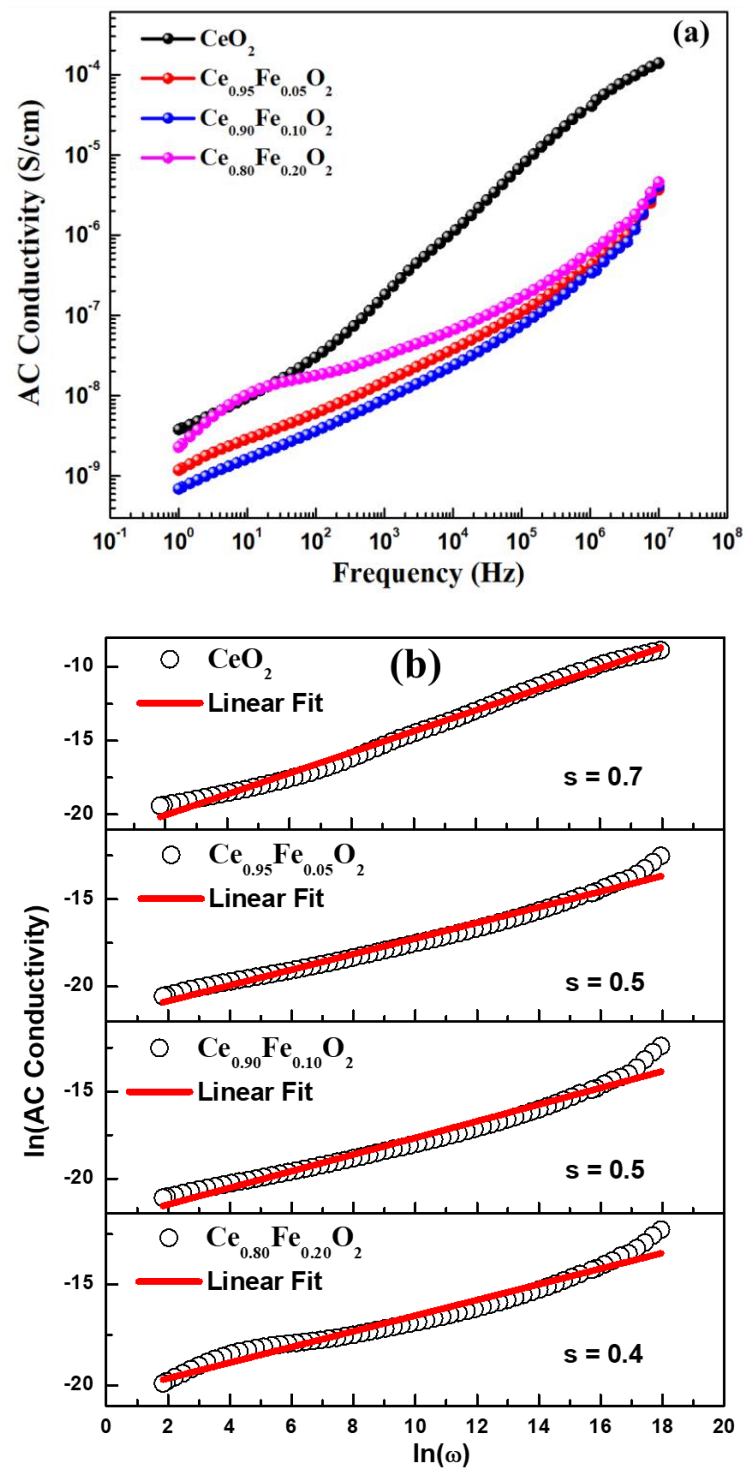


Figure 7. (a). AC conductivity vs. frequency of $\text{Ce}_{1-x}\text{Fe}_x\text{O}_{2-\delta}$, ($0 \leq x \leq 20$) NPs at room temperature. (b). Fitted $\ln(\text{AC conductivity})$ vs. $\ln(\omega)$ of $\text{Ce}_{1-x}\text{Fe}_x\text{O}_{2-\delta}$, ($0 \leq x \leq 20$) NPs at room temperature.

The NPs were evaluated for their antimicrobial activity against methicillin-resistant *S. aureus*. The results of inhibition of bacterial growth kinetics based on OD620 measurement in a concentration range of 20–50 $\mu\text{g}/\text{mL}$ of NPs are shown in Figure 8. The data exhibit the dose-dependent effect of NPs on the test strains in a concentration range of 20–50 $\mu\text{g}/\text{mL}$ and suggests a maximum cytotoxic effect with 50 $\mu\text{g}/\text{mL}$ of NPs, as shown in Figure 8. The results in Figure 9 show the NPs concentration-dependent inhibition of biofilm formation. The data revealed $81 \pm 3.5\%$ inhibition of biofilms formed by *S. aureus*

at 50 $\mu\text{g}/\text{mL}$ $\text{Ce}_{0.80}\text{Fe}_{0.20}\text{O}_2$ after 24 h of treatment. They are regarded as causative agents of many infections in humans, ranging from superficial skin suppurations to life-threatening septicaemias associated with visceral or bone infections [19]. Successful treatment becomes more challenging by the increasing prevalence of methicillin resistance and antibiotic inefficacy, when such bacteria are involved in chronic infections. Thus, NPs that induce quorum quenching could be an alternate strategy for combating biofilm-based bacterial infections by *S. aureus*, which is a potent biofilm producer, apart from conventional antibiotic therapy.

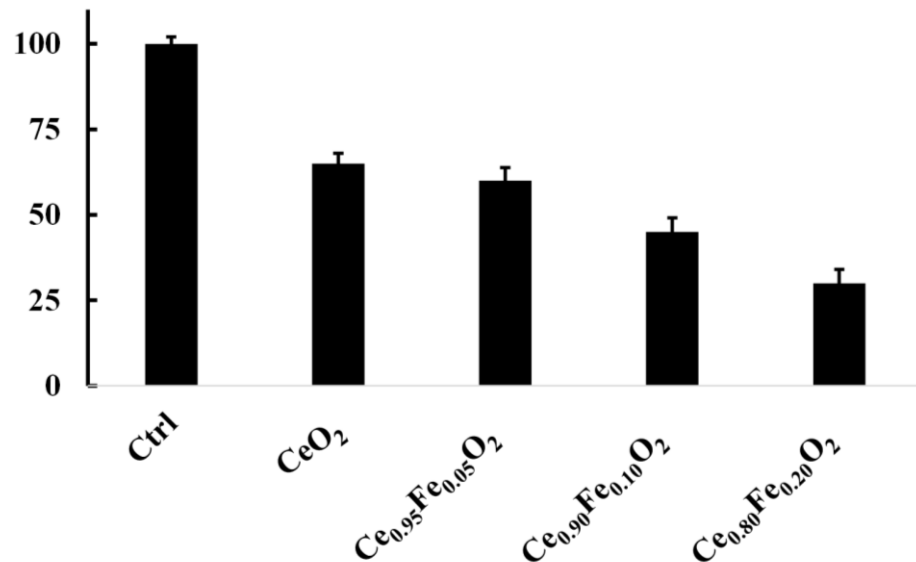


Figure 8. Bacterial growth inhibition using $\text{Ce}_{1-x}\text{Fe}_x\text{O}_{2-\delta}$, ($0 \leq x \leq 20$) NPs.

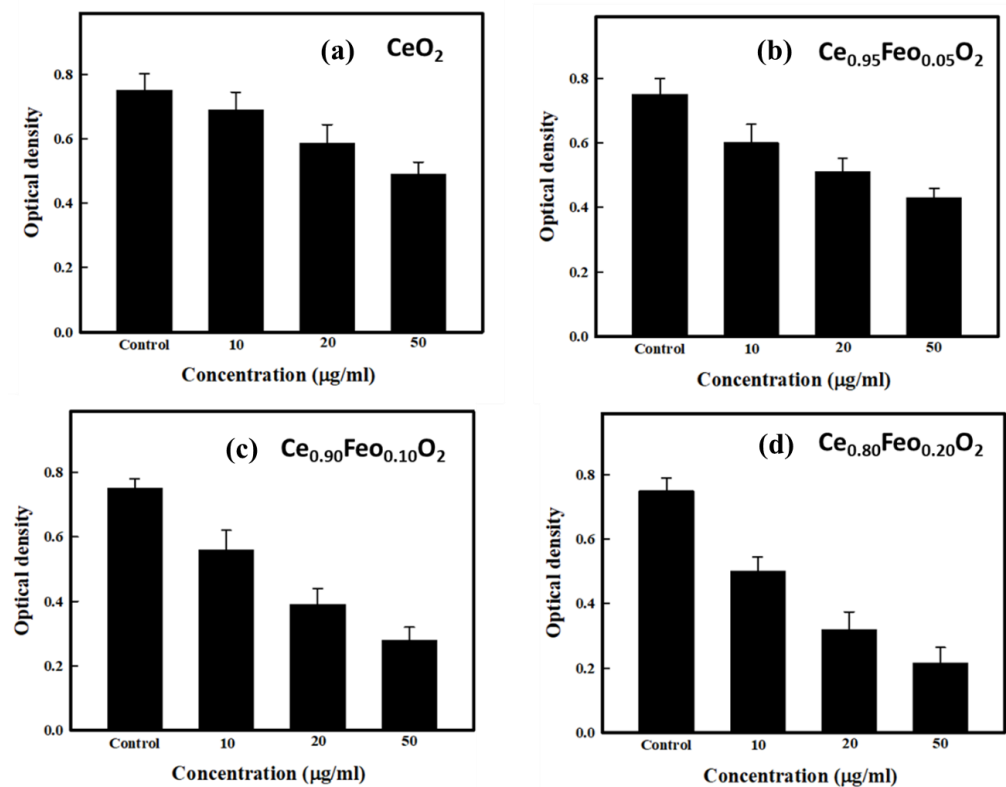


Figure 9. Antibiofilm activity of (a) CeO_2 , (b) $\text{Ce}_{0.95}\text{Fe}_{0.05}\text{O}_2$, (c) $\text{Ce}_{0.90}\text{Fe}_{0.10}\text{O}_2$, (d) $\text{Ce}_{0.80}\text{Fe}_{0.20}\text{O}_2$ NPs.

4. Conclusions

We successfully prepared $Ce_{1-x}Fe_xO_{2-\delta}$ ($0 \leq x \leq 20$) nanoparticles. The structural analysis carried out using XRD and SAED patterns showed the single-phase nature of samples. Various structural parameters such as lattice constant (a), lattice volume (V), strain (ϵ), and crystallite size were found to decrease with an increase in Fe doping. The lattice parameters and unit cell volume determined using the Rietveld refinement of the XRD were found to decrease from 7.4174 to 5.3913 Å and 158.99 to 156.80 Å³, respectively, with Fe doping content in CeO₂ nanoparticles. The crystalline size determined using the XRD pattern and TEM micrographs were observed to decrease with Fe doping in CeO₂. Selective area electron diffraction pattern also demonstrates the crystalline nature of the Fe-CeO₂ nanoparticles. The band gap calculated using Tauc plot was observed to decrease from 2.9 to 1.1 eV with Fe content in CeO₂. The Fe-doped CeO₂ nanoparticles showed good dielectric behaviour with enhanced dielectric constant and reduced AC conductivity.

Author Contributions: Conceptualization, S.K. and F.A. (Faheem Ahmed); Data curation, S.D. and K.K.; Formal analysis, S.K., F.A. (Faheem Ahmed), S.D., and N.A.; Funding acquisition, S.Y.A.; Methodology, F.A. (Fadwa Albalawi), P.A.A., S.D., R.K., and N.A.; Project administration, S.Y.A.; Validation, S.D. and F.A. (Fadwa Albalawi); Visualization, S.Y.A., F.A. (Fadwa Albalawi), and R.K.; Writing—original draft, S.K., F.A. (Faheem Ahmed), K.K., and S.D.; Writing—review and editing, F.A. (Faheem Ahmed), S.Y.A., F.A. (Fadwa Albalawi), N.A., S.D., S.K., R.K.; S.Y.A., and P.A.A. All authors have read and agreed to the published version of the manuscript.

Funding: This research was funded by Deanship of Scientific Research at King Saud University, grant number RGP-1441-543" and the APC was funded by Research Group number RGP-1441-543.

Institutional Review Board Statement: Not applicable.

Informed Consent Statement: Not applicable.

Data Availability Statement: Available on request.

Acknowledgments: Authors are grateful to the Deanship of Scientific Research at King Saud University for its funding of this research through Research Group number RGP-1441-543.

Conflicts of Interest: The authors declare no conflict of interest.

References

1. Kumar, S.; Gautam, S.; Song, T.K.; Chae, K.H.; Jang, K.W.; Kim, S.S. Electronic structure study of Co doped CeO₂ nanoparticles using X-ray absorption fine structure spectroscopy. *J. Alloys Compd.* **2014**, *611*, 329–334. [[CrossRef](#)]
2. Kumar, S.; Ahmed, F.; Anwar, M.S.; Choi, H.K.; Chung, H.; Koo, B.H. Signature of room temperature ferromagnetism in Mn doped CeO₂ nanoparticles. *Mater. Res. Bull.* **2012**, *47*, 2980–2983. [[CrossRef](#)]
3. Sharma, S.K.; Thakur, P.; Kumar, S.; Shukla, D.K.; Brookes, N.B.; Lee, C.G.; Pirotta, K.R.; Koo, B.H.; Knobel, M. Room temperature ferromagnetism in Fe-doped CeO₂ thin films grown on LaAlO₃ (001). *Thin Solid Film.* **2010**, *519*, 410–413. [[CrossRef](#)]
4. Anwar, M.S.; Kumar, S.; Ahmed, F.; Arshi, N.; Kil, G.-S.; Park, D.-W.; Chang, J.; Koo, B.H. Hydrothermal synthesis and indication of room temperature ferromagnetism in CeO₂ nanowires. *Mater. Lett.* **2011**, *65*, 3098–3101. [[CrossRef](#)]
5. Kumari, K.; Aljawfi, R.N.; Vij, A.; Chae, K.H.; Hashim, M.; Alvi, P.A.; Kumar, S. Band gap engineering, electronic state and local atomic structure of Ni doped CeO₂ nanoparticles. *J. Mater. Sci. Mater. Electron.* **2019**, *30*, 4562–4571. [[CrossRef](#)]
6. Kumari, K.; Aljawfi, R.N.; Chawla, A.K.; Kumar, R.; Alvi, P.A.; Alshoabi, A.; Vij, A.; Ahmed, F.; Abu-samak, M.; Kumar, S. Engineering the optical properties of Cu doped CeO₂ NCs for application in white LED. *Ceram. Int.* **2020**, *46*, 7482–7488. [[CrossRef](#)]
7. Soni, S.; Kumar, S.; Dalela, B.; Kumar, S.; Alvi, P.A.; Dalela, S. Defects and oxygen vacancies tailored structural and optical properties in CeO₂ nanoparticles doped with Sm³⁺ cation. *J. Alloys Compd.* **2018**, *752*, 520–531. [[CrossRef](#)]
8. Kumar, S.; Ahmed, F.; Shaalan, N.M.; Saber, O. Biosynthesis of ceo2 nanoparticles using egg white and their antibacterial and antibiofilm properties on clinical isolates. *Crystals* **2021**, *11*, 584. [[CrossRef](#)]
9. Shahin, A.M.; Grandjean, F.; Long, G.J.; Schuman, T.P. Cerium LIII-edge XAS investigation of the structure of crystalline and amorphous cerium oxides. *Chem. Mater.* **2005**, *17*, 315–321. [[CrossRef](#)]
10. Shi, H.; Hussain, T.; Ahuja, R.; Kang, T.W.; Luo, W. Role of vacancies, light elements and rare-earth metals doping in CeO₂. *Nat. Publ. Gr.* **2016**, *6*, 1–8. [[CrossRef](#)]
11. Coey, M.; Ackland, K.; Venkatesan, M.; Sen, S. Collective magnetic response of CeO₂ nanoparticles. *Nat. Phys.* **2016**, *12*, 694–699. [[CrossRef](#)]

12. Pelletier, D.A.; Suresh, A.K.; Holton, G.A.; McKeown, C.K.; Wang, W.; Gu, B.; Mortensen, N.P.; Allison, D.P.; Joy, D.C.; Allison, M.R.; et al. Effects of engineered cerium oxide nanoparticles on bacterial growth and viability. *Appl. Environ. Microbiol.* **2010**, *76*, 7981–7989. [[CrossRef](#)]
13. Alpaslan, E.; Geilich, B.M.; Yazici, H.; Webster, T.J. PH-Controlled Cerium Oxide Nanoparticle Inhibition of both Gram-Positive and Gram-Negative Bacteria Growth. *Sci. Rep.* **2017**, *7*, 1–12. [[CrossRef](#)] [[PubMed](#)]
14. Kasinathan, K.; Kennedy, J.; Elayaperumal, M.; Henini, M.; Malik, M. Photodegradation of organic pollutants RhB dye using UV simulated sunlight on ceria based TiO₂ nanomaterials for antibacterial applications. *Sci. Rep.* **2016**, *6*, 1–12. [[CrossRef](#)]
15. Farias, I.A.P.; Dos Santos, C.C.L.; Sampaio, F.C. Antimicrobial activity of cerium oxide nanoparticles on opportunistic microorganisms: A systematic review. *Biomed Res. Int.* **2018**, *2018*, 1923606. [[CrossRef](#)] [[PubMed](#)]
16. Ramasamy, M.; Lee, J. Recent Nanotechnology Approaches for Prevention and Treatment of Biofilm- Associated Infections on Medical Devices Recent Nanotechnology Approaches for Prevention and Treatment of Biofilm-Associated Infections on Medical Devices. *Biomed Res. Int.* **2016**, *2016*, 1851242. [[CrossRef](#)] [[PubMed](#)]
17. Stanic, V.; Janackovic, D.; Dimitrijevic, S.; Tanaskovic, S.B.; Mitric, M.; Pavlovic, M.S.; Krstic, A.; Jovanovic, D.; Raicevic, S. Synthesis of antimicrobial monophase silver-doped hydroxyapatite nanopowders for bone tissue engineering. *Appl. Surf. Sci.* **2011**, *257*, 4510–4518. [[CrossRef](#)]
18. Marcos, D.; Barba, F.; Miranda, M.; Guitia, F.; Torrecillas, R.; Moya, J.S. Synthesis and Antimicrobial Activity of a Silver-Hydroxyapatite Nanocomposite. *J. Nanomater.* **2009**, *2009*, 498505. [[CrossRef](#)]
19. Lakhota, S.R.; Mukhopadhyay, M.; Kumari, P. Cerium oxide nanoparticles embedded thin-film nanocomposite nanofiltration membrane for water treatment. *Sci. Rep.* **2018**, *8*, 4976. [[CrossRef](#)]
20. Malleshappa, J.; Nagabhushana, H.; Sharma, S.C.; Vidya, Y.S.; Anantharaju, K.S.; Prashantha, S.C.; Prasad, B.D.; Naika, H.R.; Lingaraju, K.; Surendra, B.S. Leucas aspera mediated multifunctional CeO₂ nanoparticles: Structural, Photoluminescent, Photocatalytic and Antibacterial properties. *Spectrochim. ACTA Part A Mol. Biomol. Spectrosc.* **2015**, *149*, 452–462. [[CrossRef](#)]
21. Ravishankar, T.N.; Ramakrishna, T.; Nagaraju, G.; Rajanaika, H. Synthesis and Characterization of CeO₂ Nanoparticles via Solution Combustion Method for Photocatalytic and Antibacterial Activity Studies. *Chem. Open* **2015**, *4*, 146–154. [[CrossRef](#)]
22. Cuahtecntzi-Delint, R.; Mendez-Rojas, M.A.; Bandala, E.R.; Quiroz, M.A.; Recillas, S.; Sanchez-Salas, J.L. Enhanced antibacterial activity of CeO₂ nanoparticles by surfactants. *Int. J. Chem. React. Eng.* **2013**, *11*, 781–785. [[CrossRef](#)]
23. Kumari, K.; Naji, R.; Katharria, Y.S.; Dwivedi, S.; Chae, K.H.; Kumar, R.; Alshoaibi, A.; Alvi, P.A.; Dalela, S.; Kumar, S. Study the contribution of surface defects on the structural, electronic structural, magnetic, and photocatalyst properties of Fe: CeO₂ nanoparticles. *J. Electron Spectros. Relat. Phenom.* **2019**, *235*, 29–39. [[CrossRef](#)]
24. Khadar, Y.A.S.; Balamurugan, A.; Devarajan, V.P.; Subramanian, R.; Kumar, S.D. Synthesis, characterization and antibacterial activity of cobalt doped cerium oxide (CeO₂:Co) nanoparticles by using hydrothermal method. *J. Mater. Res. Technol.* **2019**, *8*, 267–274. [[CrossRef](#)]
25. Nithya, P.; Sundarajan, M. Ionic liquid functionalized biogenic synthesis of AgAu bimetal doped CeO₂ nanoparticles from Justicia adhatoda for pharmaceutical applications: Antibacterial and anti-cancer activities. *J. Photochem. Photobiol. B Biol.* **2020**, *202*, 111706. [[CrossRef](#)] [[PubMed](#)]
26. Sharma, M.; Aljawfi, R.N.; Kumari, K.; Chae, K.H.; Chae, K.H.; Dalela, S.; Gautam, S.; Alvi, P.A.; Kumar, S. Investigation of local geometrical structure, electronic state and magnetic properties of PLD grown Ni doped SnO₂ thin films. *J. Electron Spectros. Relat. Phenom.* **2019**, *232*, 21–28. [[CrossRef](#)]
27. Dave, M.; Kumar, S.; Dalela, B.; Alvi, P.A.; Sharma, S.S.; Phase, D.M.; Gupta, M.; Kumar, S.; Dalela, S. Interplay of structural, optical, and magnetic properties of Ce_{1-x}Nd_xO_{2-δ} nanoparticles with electronic structure probed using X-ray absorption spectroscopy. *Vacuum* **2020**, *180*, 1–13. [[CrossRef](#)]
28. Kumar, S.; Kim, G.W.; Koo, B.H.; Sharma, S.K.; Knobel, M.; Chung, H.; Lee, C.G. Structural and magnetic study of a dilute magnetic semiconductor: Fe doped CeO₂ nanoparticles. *J. Nanosci. Nanotechnol.* **2011**, *11*, 555–559. [[CrossRef](#)]
29. Brito, P.C.A.; Santos, D.A.A.; Duque, J.G.S.; Macêdo, M.A. Structural and magnetic study of Fe-doped CeO₂. *Phys. B Condens. Matter* **2010**, *405*, 1821–1825. [[CrossRef](#)]
30. Psarras, G.C. *Fundamentals of Dielectric Theories*; Elsevier Inc.: Amsterdam, The Netherlands, 2018; ISBN 9780128132159.
31. Arya, A.; Sharma, A.L. Structural, Electrical Properties and Dielectric Relaxation in Na + Ion Conducting Solid Polymer Electrolyte. *J. Phys. Condens. Matter* **2018**, *30*, 165402. [[CrossRef](#)] [[PubMed](#)]
32. Havriliak, S.; Negami, S. A Complex Plane Analysis of a-Dispersions in Some Polymer Systems. *J. Polym. Sci. Part C* **1966**, *14*, 99–117. [[CrossRef](#)]
33. Feldman, Y.; Puzenko, A.; Ryabov, Y. *Fractals, Diffusion, and Relaxation in Disordered Complex Systems: A Special Volume of Advances in Chemical Physics*; John Wiley Sons, Inc.: Hoboken, NJ, USA, 2006; Chapter 1; Volume 133, pp. 1–126. [[CrossRef](#)]
34. Kumari, A.; Kumari, K.; Ahmed, F.; Alshoaibi, A.; Alvi, P.A.; Dalela, S.; Ahmad, M.M.; Aljawfi, R.N.; Dua, P.; Vij, A.; et al. Influence of Sm doping on structural, ferroelectric, electrical, optical and magnetic properties of BaTiO₃. *Vacuum* **2021**, *184*, 109872. [[CrossRef](#)]
35. Bandyopadhyay, A.; Sarkar, B.J.; Sutradhar, S.; Mandal, J.; Chakrabarti, P.K. Synthesis, structural characterization, and studies of magnetic and dielectric properties of Gd³⁺ doped cerium oxide (Ce_{0.90}Gd_{0.10}O_{2-δ}). *J. Alloy. Compd.* **2021**, *865*, 158838. [[CrossRef](#)]
36. Elliott, S.R. A.c. conduction in amorphous chalcogenide and pnictide semiconductors. *Adv. Phys.* **1987**, *36*, 135–218. [[CrossRef](#)]

37. Coondoo, I.; Panwar, N.; Rafiq, M.A.; Puli, V.S.; Rafiq, M.N.; Katiyar, R.S. Structural, dielectric and impedance spectroscopy studies in $(\text{Bi}_{0.90}\text{R}_{0.10})\text{Fe}_{0.95}\text{Sc}_{0.05}\text{O}_3$ [R = La, Nd] ceramics. *Ceram. Int.* **2014**, *40*, 9895–9902. [[CrossRef](#)]
38. Kumar, S.; Alimuddin, A.; Kumar, R.; Thakur, P.; Chae, K.H.; Angadi, B.; Choi, W.K. Electrical transport, magnetic, and electronic structure studies of $\text{Mg}_{0.95}\text{Mn}_{0.05}\text{Fe}_{2-2x}\text{Ti}_{2x}\text{O}_{4\pm\delta}$ (0_x_0.5) ferrites. *J. Phys. Condens. Matter* **2007**, *19*, 476210. [[CrossRef](#)]
39. Kumar, S.; Kumari, K.; Alharthi, F.A.; Ahmed, F.; Aljawfi, R.N.; Alvi, P.A.; Kumar, R.; Hashim, M.; Dalela, S. Investigations of TM (Ni, Co) doping on structural, optical and magnetic properties of CeO_2 nanoparticles. *Vacuum*. **2020**, *181*, 109717. [[CrossRef](#)]
40. Kumar, S.; Kumari, K.; Alvi, P.A.; Dalela, S. Study of the electronic structure of $\text{Ce}_{0.95}\text{Fe}_{0.05}\text{O}_{2-\delta}$ thin film using X-ray photoelectron spectroscopy. *J. Electron Spectrosc. Relat. Phenom.* **2021**, *250*, 147073. [[CrossRef](#)]
41. Heikes, R.R.; Johnston, W.D. Mechanism of Conduction in Li Substituted Transition Metal Oxides. *J. Chem. Phys.* **1957**, *26*, 582. [[CrossRef](#)]